

Large Eddy Simulation of Boundary Layer Transition Mechanisms in a Gas-Turbine Compressor Cascade

Ashley D. Scillitoe¹

CFD Laboratory,
Department of Engineering,
University of Cambridge,
Cambridge CB2 1PZ, UK
e-mail: as2341@cam.ac.uk

Paul G. Tucker

CFD Laboratory,
Department of Engineering,
University of Cambridge,
Cambridge CB2 1PZ, UK

Paolo Adami

CFD Methods,
Rolls-Royce Deutschland,
Eschenweg 11,
Blankenfelde-Mahlow 15827, Germany

Large eddy simulation (LES) is used to explore the boundary layer transition mechanisms in two rectilinear compressor cascades. To reduce numerical dissipation, a novel locally adaptive smoothing (LAS) scheme is added to an unstructured finite volume solver. The performance of a number of subgrid scale (SGS) models is explored. With the first cascade, numerical results at two different freestream turbulence intensities (T_i 's), 3.25% and 10%, are compared. At both T_i 's, time-averaged skin-friction and pressure coefficient distributions agree well with previous direct numerical simulations (DNS). At $T_i = 3.25\%$, separation-induced transition occurs on the suction surface, while it is bypassed on the pressure surface. The pressure surface transition is dominated by modes originating from the convection of Tollmien–Schlichting waves by Klebanoff streaks. However, they do not resemble a classical bypass transition. Instead, they display characteristics of the “overlap” and “inner” transition modes observed in the previous DNS. At $T_i = 10\%$, classical bypass transition occurs, with Klebanoff streaks inciting turbulent spots. With the second cascade, the influence of unsteady wakes on transition is examined. Wake-amplified Klebanoff streaks were found to instigate turbulent spots, which periodically shorten the suction surface separation bubble. The celerity line corresponding to 70% of the free-stream velocity, which is associated with the convection speed of the amplified Klebanoff streaks, was found to be important.

[DOI: 10.1115/1.4042023]

Introduction

In the low-pressure stages of a gas-turbine compressor, the Reynolds number is relatively low, and the flow may be transitional over a large portion of the blades [1]. This transitional behavior can significantly influence the compressor's aerodynamic performance.

Due to the reduced number of blades in modern aero-engine compressors, the suction surface boundary layers are more prone to separation. The separated shear layer becomes turbulent soon after separation and quickly reattaches. The separation bubble alters the effective blade loading distribution, thus degrading the blade's performance. At higher free-stream turbulence (FST) intensities (T_i 's), earlier transition results in shorter separation bubbles [2]. However, the increased turbulent wetted area causes profile losses. Moreover, the transitional processes on the suction surface have been found to influence the deleterious corner separations that occur close to the end walls [3], potentially leading to increased endwall losses. Wakes from upstream stages can also cause significant variations in the transition mechanisms and transition location in compressors. Adamczyk et al. [4] show that capturing these variations is vital for properly predicting the performance of a compressor stage.

In order for computational fluid dynamics (CFD) to be effectively utilized to develop new compressor designs, it is important that the CFD tools can reliably predict the effects of free-stream turbulence and migrating wakes on transition, and therefore compressor performance. This is especially challenging, since the flow

physics occurring in a compressor is complicated by leading-edge and suction-side curvature, strong pressure gradients, and the complex nature of the turbulent flow through the passages. Laminar-to-turbulent transition can be triggered by impinging wakes, unstable Tollmien–Schlichting waves, background turbulence, or a combination of these [5]. When used with a transition model (e.g., see Ref. [6]), Reynolds-averaged Navier–Stokes models are able to capture some of the first-order effects of transition. However, it is well known that they struggle to capture the more detailed physics, especially when there is no spectral gap between the modeled and resolved unsteadiness.

An alternative CFD approach to Reynolds-averaged Navier–Stokes is direct numerical simulation (DNS), where all the scales of turbulence are directly simulated. Zaki et al. [5] used DNS to study the interaction of grid-generated free-stream turbulence with the boundary layers in a compressor cascade. Although accurate, for the foreseeable future, DNS is only suited to “one-off” simulations due to its extreme computational cost. Lardeau et al. [2] and Leggett et al. [7] have performed large eddy simulations (LES) of the same case at a fraction of the cost. In both cases, good agreement was obtained with time-averaged quantities from the DNS of Zaki et al. [5]. However, the extent to which the more detailed physics involved in transition captured is less clear. This paper aims to investigate this with the following two studies:

- (1) The mechanisms of laminar-to-turbulent transition in a compressor cascade will be examined at two different free-stream T_i 's. Comparisons will be made to the DNS of Zaki et al. [5] to determine if the same transition mechanisms are observed at both T_i 's.
- (2) The wake-induced transition will be simulated in a compressor cascade, to determine to what extent the observed physics match that seen in previous experiments, such as the turbine cascade experiments of Coull and Hodson [8].

¹Corresponding author.

Contributed by the International Gas Turbine Institute (IGTI) of ASME for publication in the JOURNAL OF TURBOMACHINERY. Manuscript received September 18, 2018; final manuscript received November 14, 2018; published online January 22, 2019. Editor: Kenneth Hall.

Table 1 Geometrical and inflow parameters for the two compressor cascades

	Cascade 1	Cascade 2
Blade profile	NACA-65-k48	Controlled diffusion aerofoil
Chord length, c	220 mm	151.5 mm
Axial chord length, C_x	204 mm	146.5 mm
Reynolds number,	1.38×10^5	2.3×10^5
$Re_c = U_1 c / \nu$		
Aspect ratio	1.36	1.32
Inflow incidence	-6.0 deg	0.0 deg
Flow turning	36.0 deg	33.0 deg

It is important to understand how well LES can capture the finer details of transition in compressors. This will provide confidence that LES may be used to further develop transition models and correlations for application in complex compressor flows.

Flow Configurations

The two linear compressor blade cascades detailed in Table 1 are simulated in this paper. Although not up-to-date profiles, both aerofoil cascades have been used in many studies [9–12] to represent the compressor stator blades found in an axial flow gas-turbine compressor. Cascade 1 consists of NACA-65 aerofoils and was tested experimentally by Hilgenfeld and Pfitzner [12]. This cascade was also simulated at a lower Re_c using DNS by Zaki et al. [5] and using LES by Lardeau et al. [2]. Cascade 2 is a linear controlled diffusion aerofoil cascade investigated experimentally by Gbadebo [11].

To discretize each cascade, a standard H–O–H mesh topology is used. For cascade 1, a baseline mesh is designed to have a nondimensional spacing of $\Delta^+ < 50/1/15$ in the tangential/normal/spanwise directions at the wall. These grid resolutions are well within the recommended values for wall-resolved LES given by Piomelli and Chasnov [13]. The resulting O-block for this mesh has $690 \times 45 \times 136$ points in the streamwise/pitchwise/spanwise directions, leading to a total of 9.3M grid points, including the H-blocks. To check for mesh dependence, a finer mesh with double the number of streamwise and spanwise grid points (37.4M in total) is also used for cascade 1 (LES case C6 in Table 2).

The cascade 2 mesh is designed to meet the same nondimensional wall spacing limits as the baseline mesh for cascade 1. Due to the higher Reynolds number of cascade 2 the resulting number of grid points is higher, with 17.6 M in total. More details of the meshes used can be found in Ref. [3].

The blades are represented with no-slip walls, and standard velocity inlet and static pressure outlet boundaries are enforced. Downstream of the blade, a sponge zone is used to prevent reflections from the outflow boundary. Pitchwise periodicity is enforced with periodic boundaries at midpitch. Following the DNS of Zaki et al., a spanwise extent of $0.2C_x$ is used for all cases, with periodicity also enforced in this direction.

The LES cases run for cascade 1 are listed in Table 2. A number of different cases are run to examine the influence of free-stream turbulence and the sensitivity to the subgrid scale (SGS) model. The free-stream turbulence intensities are chosen to match the DNS of Zaki et al. [5]. Two cases are run for cascade 2, with and without incoming turbulent wakes, in order to examine their influence on the boundary layer transition. For both these cases, the free-stream Ti is set at 1.5%, in order to match the experiments of Gbadebo [11]. The incoming turbulent scales were not measured in the experiment, and the integral length scale is arbitrarily set to $L = 0.06C_x$ for cascade 2.

Numerical Method

The code used is a modified version of the Rolls-Royce CFD code HYDRA [14]. It is a second-order unstructured finite volume code, which has been successfully used for a number of low pressure turbine LES studies [15].

Numerical Scheme. Originally, HYDRA solved the compressible Navier–Stokes equations. However, to improve the code’s performance at low Mach numbers, it has been modified to use an artificial compressibility method [16]. This involves solving a modified form of the Navier–Stokes equations

$$\frac{\partial \mathbf{D}}{\partial \zeta} + \Gamma_t \frac{\partial \mathbf{D}}{\partial t} + \frac{\partial}{\partial x_i} \mathbf{R}(\mathbf{D}) = 0 \quad (1)$$

where

$$\mathbf{D} = \begin{Bmatrix} p \\ \rho u_1 \\ \rho u_2 \\ \rho u_3 \end{Bmatrix}, \quad \mathbf{R}(\mathbf{D}) = \begin{Bmatrix} \beta u_i \\ \rho u_1 u_i + p \delta_{i1} + 2\mu S_{1i} - \rho \bar{u}_1' \bar{u}_j'_{SGS} \\ \rho u_2 u_i + p \delta_{i2} + 2\mu S_{2i} - \rho \bar{u}_2' \bar{u}_j'_{SGS} \\ \rho u_3 u_i + p \delta_{i3} + 2\mu S_{3i} - \rho \bar{u}_3' \bar{u}_j'_{SGS} \end{Bmatrix}$$

β is the pseudo-compressibility constant, ζ refers to pseudo-time, $S_{ij} = 1/2(\partial u_i / \partial x_j + \partial u_j / \partial x_i)$ is the instantaneous strain rate tensor, and $\Gamma_t = \text{diag}[0, 1, 1, 1]$. Dual time stepping is used to advance the solution in real time. Second-order backward-differencing is used to approximate the $\partial \mathbf{D} / \partial t$ term in Eq. (1). During pseudo-time, a three-stage Runge–Kutta scheme is used to drive the $\partial \mathbf{D} / \partial \zeta$ term toward zero, which ensures that a divergence-free velocity field is satisfied. The density ρ and viscosity μ are now user-specified constants, chosen to give the desired Reynolds number.

HYDRA uses the Roe flux-differencing method [17] to solve for the inviscid flux through each control volume face. This is essentially central differencing, smoothed by some upwinding scaled by a smoothing constant ε_2

$$\mathbf{F}_{ij}^{I,S} = \underbrace{\frac{1}{2} (\mathbf{F}_{ij}^I(\mathbf{Q}_i) + \mathbf{F}_{ij}^I(\mathbf{Q}_j))}_{\text{Central differencing}} - \underbrace{\frac{1}{2} \varepsilon_2 |\mathbf{A}_{ij}| (\mathbf{L}_i^{lp} - \mathbf{L}_j^{lp})}_{\text{Upwinding}} \quad (2)$$

\mathbf{F}_{ij}^I and $\mathbf{F}_{ij}^{I,S}$ are the original and smoothed inviscid fluxes through a cell face, $|\mathbf{A}_{ij}|$ is the flux Jacobian, and \mathbf{L}_i^{lp} is a Laplacian operator.

For eddy resolving simulations, it is important to minimize the ε_2 smoothing to prevent excessive numerical dissipation. However, reducing the smoothing too much results in dispersive errors, seen as wiggles in the solution. To avoid the need for manual tuning of the smoothing constant, some authors, like Tajallipour et al. [18], propose locally adaptive smoothing (LAS) schemes. Such schemes locally adapt the numerical smoothing across each e_{ij} edge, according to the local magnitude of any wiggle across the edge. Wiggles are said to be present if the following two conditions are met:

Table 2 Cases simulated for cascade 1

Case	Inflow turbulence			
	Ti (%)	L/C_x	SGS model	Mesh
C1	3.25	0.03	σ	Baseline
C2	3.25	0.06	σ	Baseline
C3	3.25	0.06	WALE	Baseline
C4	3.25	0.06	SM	Baseline
C5	10.0	0.06	σ	Baseline
C6	3.25	0.03	σ	Fine

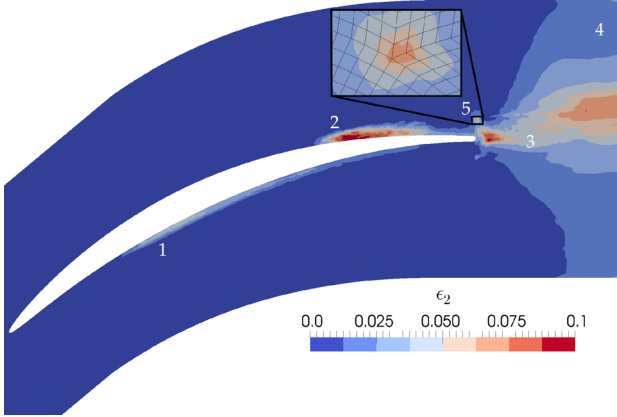


Fig. 1 Contours of converged ε_2 smoothing field with LASW scheme, for case C1

$$\begin{aligned}\theta_i(t) &= (\phi_i - \phi_{i-1})(\phi_j - \phi_i) < \theta_t < 0 \\ \theta_j(t) &= (\phi_{j+1} - \phi_j)(\phi_j - \phi_i) < \theta_t < 0\end{aligned}\quad (3)$$

where ϕ is the velocity or pressure, and θ_t is the target wiggle magnitude (i.e., $\theta_t = 0$). To adjust ε_2 , Tajallipour et al. [18] propose using a proportional controller, $\Delta\varepsilon_2(t) = [\theta_t - \min(\theta_i(t), \theta_j(t))] \alpha$. However, preliminary tests on a forced isotropic turbulence test case [19] showed the controller to be overly sensitive to the gain parameter α .

To improve the LAS scheme, the locally adaptive smoothing with windowing (LASW) procedure is introduced. The average wiggle magnitude is evaluated over the time window T_w

$$\theta_w = \frac{1}{T_w} \int_{t_w=0}^{t_w=T_w} \theta(t_w) dt_w \quad (4)$$

where $\theta = \sqrt{|\max(\theta_i(t), \theta_j(t))|}$ is the wiggle magnitude. The proportional controller, $\Delta\varepsilon_2(t) = (\theta_w(t) - \theta_t)\alpha$, is only applied when $t_w \geq T_w$. Then, t_w and θ_w are zeroed ready for the next window. Windowing provides a less intermittent error signal for the proportional controller and avoids the increasing insensitivity to the error signal that an integral controller would suffer from. As long as T_w is large enough, the ε_2 field is found to converge to a steady-state, independent of the gain parameter α . The resulting ε_2 field for LES case C1 is shown in Fig. 1. Low dissipation central differencing is used in most of the domains, with small amounts of numerical smoothing added where necessary to prevent wiggles. The LASW scheme is used for all the simulations described in this paper, with $T_w = 0.2T^*$, $\alpha = 1.0$, and $\theta_t = 0.0$.

Subgrid Scale Modeling. The modeled (unresolved) stresses in Eq. (1) are obtained via the Boussinesq approximation

$$-\rho \overline{u'_i u'_j}_{SGS} = 2\mu_{sgs} \left(S_{ij} - \frac{1}{3} S_{kk} \delta_{ij} \right) \quad (5)$$

where the SGS viscosity μ_{sgs} is given by a SGS model. A number of SGS models are used in this paper, the first is the Smagorinsky–Lilly (SM) model [20], which defines the SGS viscosity as

$$\mu_{sgs} = \rho \Delta_{sgs}^2 \sqrt{2S_{ij} S_{ij}} \quad (6)$$

To prevent high aspect ratio cells near walls leading to excessively high μ_{sgs} values, Schumann's near-wall limiter [21], $\Delta_{sgs} = \min(C_s \Delta_{vol}, \kappa d)$, is used.

The second SGS model used is the wall-adapting-local-eddy viscosity (WALE) model introduced by Nicoud and Ducros [22]

$$\mu_{sgs} = \rho (C_w \Delta_{vol})^2 \frac{\left(S_{ij}^d S_{ij}^d \right)^{3/2}}{\left(S_{ij} S_{ij} \right)^{5/2} + \left(S_{ij}^d S_{ij}^d \right)^{5/4}} \quad (7)$$

The $S_{ij}^d S_{ij}^d$ term is based on both strain and vorticity and is formulated to give zero SGS viscosity in pure shear regions such as a laminar boundary layer.

The final model tested is the σ model, also proposed by Nicoud et al. [23]. It bases the SGS viscosity on the singular values ($\sigma_1, \sigma_2, \sigma_3$) of the resolved gradient tensor

$$\mu_{sgs} = \rho (C_\sigma \Delta_{vol})^2 \frac{\sigma_3 (\sigma_1 - \sigma_2)(\sigma_2 - \sigma_3)}{\sigma_1} \quad (8)$$

The WALE and σ model constants recommended by Nicoud and Ducros [22] and Nicoud et al. [23] ($C_w = 0.5$ and $C_\sigma = 1.35$) are used. For isotropic decaying turbulence, these constants give dissipation equal to using the Smagorinsky model with $C_s \approx 0.165$. This value is chosen for the Smagorinsky model here.

Time-Dependent Inflow Conditions. To represent FST, isotropic turbulence generated using an open-source synthetic turbulence tool [24] is added onto the mean inflow velocity boundary condition. The tool generates a divergence-free velocity field that matches a given energy spectrum. In this case, it is the von Kármán-Pao spectrum

$$E(\kappa) = \alpha \frac{u'^2}{\kappa_e} \frac{(\kappa/\kappa_e)^4}{[1 + (\kappa/\kappa_e)]^{17/6}} \exp \left[-2 \left(\frac{\kappa}{\kappa_\eta} \right)^2 \right] \quad (9)$$

where u' is the rms value of the velocity fluctuations, κ_e is related to the wavenumber of maximum energy ($\kappa_p = \sqrt{12/5\kappa_e}$), and $\kappa_\eta = \varepsilon^{1/4} \nu^{-3/4}$ is the Kolmogorov wave number. As recommended by Bailly and Juve [25], for isotropic turbulence, $\alpha = 1.453$, and $\varepsilon = u'^3/L$ with L being the integral length scale $L = 0.746834/\kappa_e$.

The turbulent wake data are obtained from a separate simulation [26], which has been kindly provided by Xiaohua Wu. This datum was generated by initially “fusing” two “half-channel flow” simulations ($Re_b = 3300$) and allowing the solution to develop until it reaches a statistically steady-state.

The wake data are scaled by the parameters given in Table 3. These values are chosen so that the incoming wakes are representative of those seen by stator stages in a gas turbine engine. The wake data are applied to the inflow using the procedure given in Wu et al. [26].

Simulation Time/Cost. The time-step is set to give $CFL_{max} \approx 0.8$, and a flow-through time (T^*) equates to approximately 10,000 time-steps. The simulations without wakes were run for $4T^*$ to clear the initial transients, and a further $10T^*$ to collect statistics. The simulation with wakes was run for six wake passing periods ($\tau = 1.09T^*$) to establish a periodic flow, followed by 28τ to obtain well converged-phase averages. All time- and phase-averaged data are also averaged in the spanwise direction.

Table 3 Parameters of incoming turbulent wake

Wake parameter	Value
Mean velocity deficit	$0.2U_0$
Half-width	$0.05C_x$
Vertical separation	$0.9P$ (P is blade pitch)
Cycle velocity	$0.8U_1$
Wake passing period, τ_w	$1.09C_x/U_1$
Reduced frequency, $f_r = \frac{1}{\tau_w} \frac{C_x}{U_{TE}}$	1.2

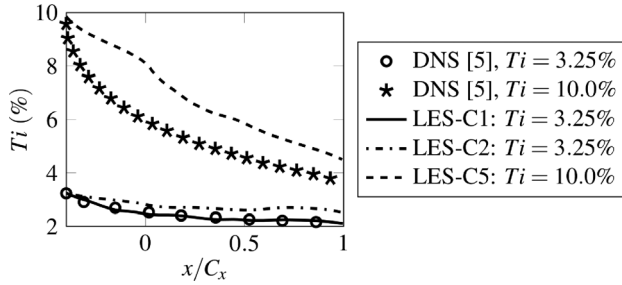


Fig. 2 Turbulence intensity, Ti , at midpitch of cascade 1

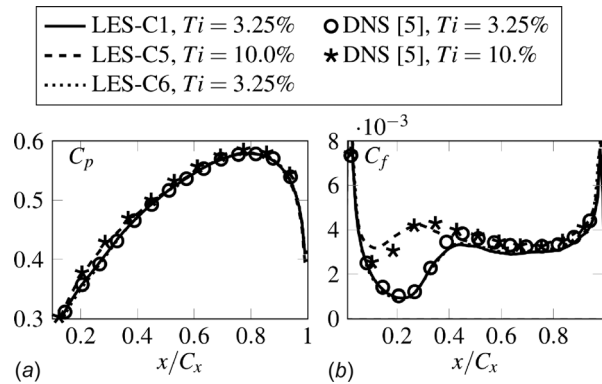


Fig. 3 Time-averaged pressure and skin friction coefficients on the pressure surface of cascade 1: (a) pressure coefficient, C_p and (b) skin friction coefficient, C_f

Simulations were run on 128–512 processing cores on ARCHER, the UK’s National HPC facility. ARCHER is a Cray XC30 MPP supercomputer consisting of 4920 compute nodes, each with two 12-core Intel Ivy Bridge Processors. Simulations required 1–2 kCPU hours per T^* .

Influence of Free-Stream Turbulence Intensity on the Transition Mechanisms

For the majority of the cases in Table 2, the integral length scale of the free-stream turbulence was chosen as $L = 0.06C_x$ in order to match the DNS [5]. The turbulence intensity is defined as $Ti = \sqrt{u'_i u'_i} / 3U_1^2$, where U_1 is the inflow bulk velocity, and fluctuating quantities are obtained through the standard Reynolds

decomposition, $f' = \bar{f} - f$. Ti at midpitch in a number of LES cases is compared to the DNS in Fig. 2. It is found that $L = 0.06C_x$ results in a slower decay rate of Ti compared to the DNS. This may be due to differences in the definition of the integral length scale used by Zaki et al. [5] and that used in the synthetic turbulence method of Saad et al. [24], or due to differences in the energy spectra of the FST.

To enable a fair comparison with the DNS, one additional case (C1) was run with a smaller inflow integral length scale $L = 0.03C_x$. Figure 2 shows that the FST decay rate is in much closer agreement with the DNS in this case. Despite the lower FST decay rate in the other cases, a comparison of cases C1 and C5 still provides a valid basis to examine the influence of free-stream turbulence on the transition mechanisms.

Pressure Surface Transition Mechanisms—Moderate Free-Stream Turbulence Intensity. Figure 3 shows the pressure surface distributions of the time-averaged pressure coefficient, $C_p = (\bar{p} - \bar{p}_1) / ((1/2)\rho U_1^2)$, and the time-averaged skin friction coefficient, $C_f = \tau_w / ((1/2)\rho U_1^2)$. τ_w is the wall shear stress, and \bar{p}_1 is the time-averaged static pressure at the inflow.

From the C_p distribution in Fig. 3(a), it is clear that the FST has some effect, and this becomes more apparent in the C_f distribution in Fig. 3(b). In the absence of free-stream perturbations, the suction surface flow separates (indicated by $C_f \leq 0$) in the laminar ($Ti = 0\%$ case) DNS case of Zaki et al. [5]. On the other hand, in the present cases where free-stream perturbations are present, the boundary layer is transitioned to turbulence and the flow is prevented from separating.

Despite the slightly premature transition in the $Ti = 10.0\%$ case (due to the slower decay of the incoming FST, seen in Fig. 2), the effect of FST on the time-averaged flow is generally well captured by the LES. However, as discussed in the Introduction section, breakdown to turbulence in turbomachinery flows can be caused by a number of different mechanisms. Now, the pressure surface transition mechanisms will be examined in more detail to see if the finer physics are properly captured. Cases C6 and C1 are in close agreement in Fig. 3, suggesting that a satisfactory level of grid independence is reached with the baseline mesh for cascade 1.

In Fig. 4, the pressure surface transition process under moderate FST (case C1, $Ti = 3.25$) is visualized using iso-surfaces of Q -criterion. The locations of transition onset (X_s) and completion (X_e) are shown by the white lines. Following Zaki et al. [5], X_s is defined as the minimum C_f location in Fig. 3(b), while X_e is the point where C_f plateaus. Figure 4 shows contours of the tangential velocity perturbations, $u'_t = u'_t x_t + v'_t y_t$, at $d^+ \approx 15$ from the wall. (x_t, t_y) is the two-dimensional streamwise unit tangent,

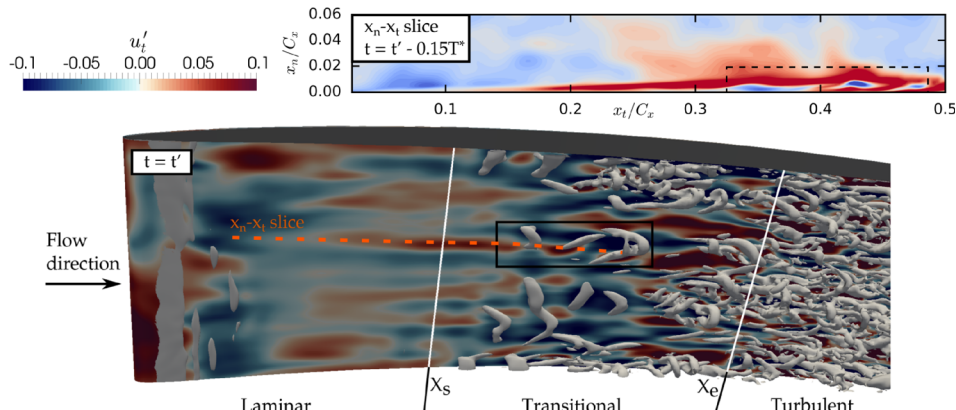


Fig. 4 Case C1. Contours of the tangential velocity perturbations on a plane inside the pressure surface boundary layer, $d^+ \approx 15$ from the wall. An iso-surface of $Q = 200U_0/C_x$ is superimposed. Also shown is an $x_n - x_t$ slice bisecting the Λ -structure, at a time instance $0.15T^*$ prior to the main image.

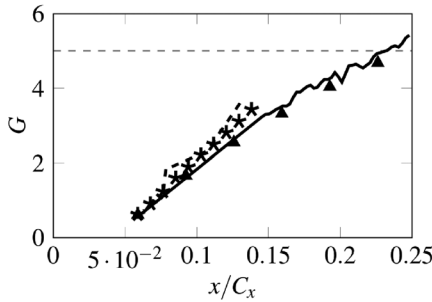
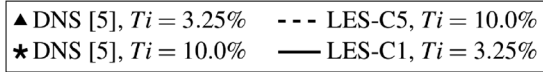


Fig. 5 Görtler number, G , (upstream of transition/separation) on the pressure surface

and $d^+ = d\sqrt{\tau/\rho}/\mu$ is the nondimensional wall distance. These contours show that in the laminar region ($x < X_s$), the boundary layer is dominated by streaks of strong forward and backward tangential velocity. To determine whether these streaks are related to Görtler instabilities, the Görtler number, $G \equiv \sqrt{\theta/R}(\bar{u}_e\theta/\nu)$, is plotted in Fig. 5. Here, R is the local radius of curvature of the wall, θ is the boundary layer momentum thickness, and U_e is the edge of boundary layer velocity. Saric [27] found that the boundary layer on a concave surface becomes unstable at $G \sim 0.3$, but Görtler vortices are not detected until $G \sim 5 - 6$. Figure 5 shows that $G > 5$ for only a very small streamwise distance before transition, and thus Görtler vortices are not likely to occur. Zaki et al. [5] also failed to detect Görtler vortices, and instead showed that these streaks are Klebanoff distortions forced by the low-frequency component of the FST.

The natural transition of boundary layers via Tollmien-Schlichting (TS) waves is often bypassed when $Ti > 1\%$ [28]. However, Zaki et al. [5] found that at $Ti = 3.25\%$, the instability modes observed on the pressure surface do not resemble the traditional bypass mechanism. Instead, two distinct near-wall modes were found. These modes were also observed in the present LES case and are visualized in Fig. 6. Although these modes are not streak instabilities, they are influenced by the Klebanoff streaks. In both modes, vortical structures develop in (or slightly upstream of) the transitional region ($X_s < x < X_e$), and then breakdown to turbulence.

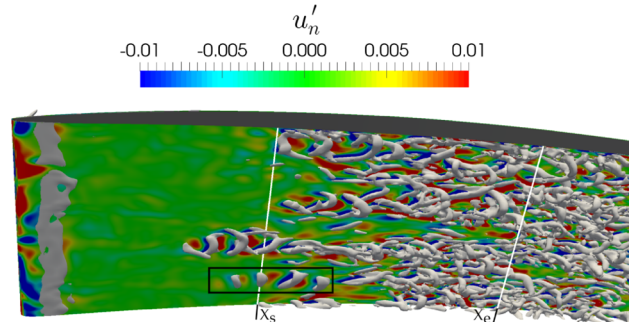


Fig. 7 Case C1. Contours of the normal velocity perturbations, u'_n , on the $d^+ \approx 15$ pressure surface plane. An iso-surface of $Q = 200U_0/C_x$ is superimposed.

The Inner Mode. The so-called *inner mode* structure shown in Fig. 6(a) is also highlighted in Fig. 4. These strong vortices are referred to as Λ -vortices due to their shape. Their presence hints at a natural transition mechanism. However, as noted by Zaki et al. [5], they cannot be independent of the streaks, as they would then be observed homogeneously across the blade span. The structures' spanwise size are not directly related to the streaks; in LES case C1 the average spanwise wavelength of the streaks is approximately $0.015C_x$, but the Λ structures' width ranges from $0.02C_x$ to $0.035C_x$.

Figure 4 also shows the u'_t field on a wall tangential-normal ($x_t - x_n$) plane bisecting the Λ -structure, at a time $0.15T^*$ prior to that in the main image. The disturbance (highlighted by the dashed box) is initiated below the forward-velocity streak, hence the name inner mode. Similar behavior is observed in the DNS [5].

The Overlap Mode. The second mode observed is the overlap mode, shown in Fig. 6(b). This mode is also an inner instability. However, it is characterized by a significantly shorter spanwise wavelength than the inner mode. Here, the instability has the same width as the host streak.

The inception of these instabilities can be easily observed by examining contours of wall-normal velocity fluctuations ($u'_n = -u't_y + v't_x$), like those in Fig. 7. The instability typically starts some distance upstream of X_s . The $x_n - x_t$ slice in Fig. 8 shows that the instabilities are located where the downstream edge of a high speed streak overlaps with the upstream edge of a

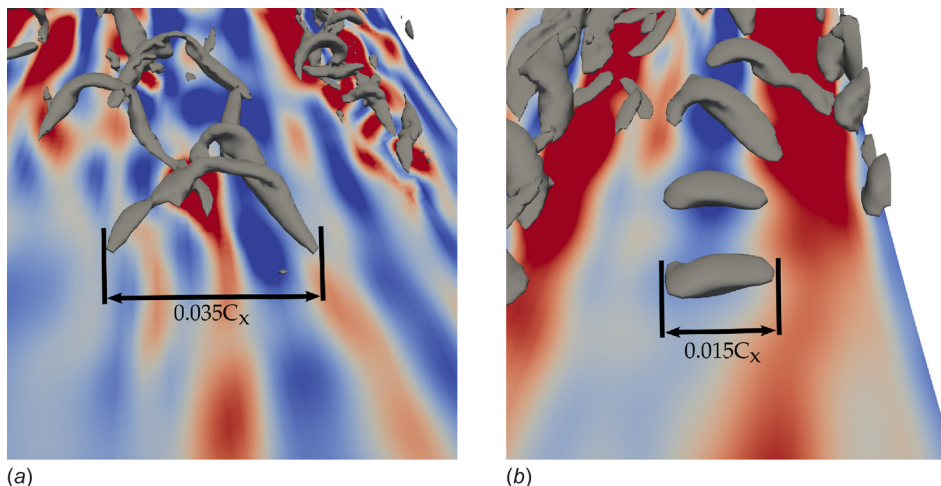


Fig. 6 Case C1. Two of the vortical structures present on the pressure surface, visualized using iso-surfaces of $Q = 200U_0/C_x$. Case C1. Contours of $-0.1 < u_t < 0.1$ are also shown: (a) inner mode Λ -structure and (b) overlap mode structures.

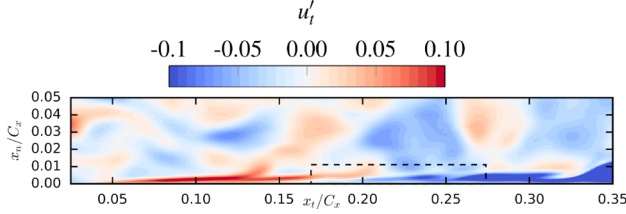


Fig. 8 Case C1. Contours of the tangential velocity perturbations, u'_t , on an $x_t - x_n$ plane bisecting the overlap mode structure highlighted in Fig. 7. The time is 0.17^* prior to that in Fig. 7.

low speed streak. Again, this behavior is in agreement with the DNS results of Zaki et al. [5].

Suction Surface Transition Mechanisms—Moderate Free-Stream Turbulence Intensity. The suction surface C_p and C_f distributions are plotted in Fig. 9. Generally, as for the pressure surface, the overall effect of Ti is well captured by the LES. Again, cases C6 and C1 are in close agreement, suggesting that a satisfactory level of grid independence is reached with the baseline mesh. Unlike for the pressure surface, the flow separates in the $Ti = 3.25\%$ case here.

In Fig. 10, the suction surface in LES case C1 ($Ti = 3.25$) is displayed. Similarly to the pressure surface, a streaky laminar region is visible. The laminar boundary layer undergoes separation in the adverse pressure gradient region close to the time-averaged separation location x_s , and Kelvin–Helmholtz (K–H) rolls develop. Transition has still not occurred at $x_s = 0.46$, which is significantly downstream from the pressure surface transition location ($X_s = 0.22$). This is explained by the fact that Klebanoff streaks, a precursor for transition here, are found to amplify faster in the presence of an adverse pressure gradient [29].

In the laminar DNS case [5], the K–H rolls remain laminar and convect downstream, maintaining a separation region in their shadow. However, in the $Ti = 3.25\%$ DNS case, the K–H rolls are quickly destabilized by the free-stream turbulence. The rolls break down and are followed by turbulent reattachment of the boundary layer. This process is well captured by the LES; an attached turbulent boundary layer is visible after x_r in Fig. 10, and the LES C_f agrees well with the DNS at $x \geq 0.72$ in Fig. 9(b).

The time-averaged C_f profile in Fig. 9(b) suggests that a free-stream Ti of 3.25% has little influence on the separation location. However, the instantaneous separation region, shown by the black iso-surface in Fig. 10, shows that the separation location varies in time. This is due to the Klebanoff streaks; separation is shifted upstream where elongated u'_t contours are negative, and downstream where they are positive. This effect is well captured by the

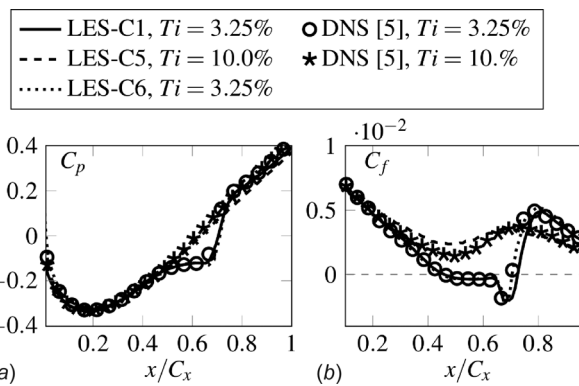


Fig. 9 Pressure and skin friction coefficients on the suction surface of cascade 1: (a) pressure coefficient, C_p and (b) skin friction coefficient, C_f

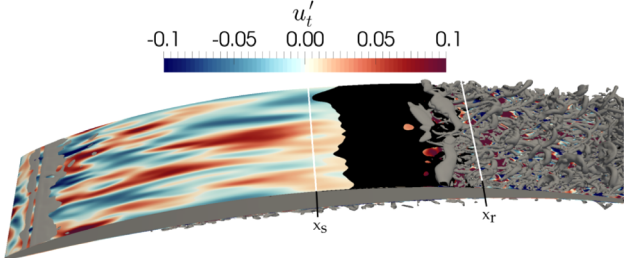


Fig. 10 Case C1. Contours of the tangential velocity perturbations, u'_t , on a plane inside the suction surface boundary layer $d^+ \approx 15$ from the wall. Iso-surfaces of $Q = 300 U_0 / C_x$ (gray) and $u'_t = 0$ (black) are superimposed.

LES, with the resulting K–H rolls seen to be more three-dimensional than in the laminar DNS case of Zaki et al. [5].

Transition Mechanisms at High Free-Stream Turbulence Intensity. At the higher free-stream Ti of 10% , a streaky laminar region is visible. The laminar boundary layer undergoes separation in the adverse pressure gradient region close to the time-averaged separation location x_s , and Kelvin–Helmholtz (K–H) rolls develop. Transition has still not occurred at $x_s = 0.46$, which is significantly downstream from the pressure surface transition location ($X_s = 0.22$). This is explained by the fact that Klebanoff streaks, a precursor for transition here, are found to amplify faster in the presence of an adverse pressure gradient [29].

On the pressure surface, this mechanism causes the inner and overlap transition modes to be bypassed, and the transition point moves upstream from $X_s = 0.22C_x$ with $Ti = 3.25\%$ to $X_s = 0.13C_x$ with $Ti = 10\%$, as seen in Fig. 3. On the suction surface, Fig. 9 shows there is little change in C_f in the favorable pressure gradient region, but C_f remains higher in the adverse pressure gradient region compared to in the $Ti = 3.25$ case. This higher C_f prevents the boundary layer from separating.

Sensitivity to the Subgrid Scale Model

In a previous paper by the authors [3], the sensitivity to the SGS models was examined. In the present section, a more in-depth study on the effect of the different SGS models is presented. In Fig. 12, the C_f distributions for cases C2, C3, and C4 are plotted, along with the LES results of Lardeau et al. [2]. The WALE and σ SGS model predictions are seen to compete well with the Dynamic Smagorinsky SGS model predictions of Lardeau et al. [2].

On the other hand, the SM model performs poorly on both surfaces. On the pressure surface, the inner and overlap instabilities occur much later, suggesting excessive damping from the

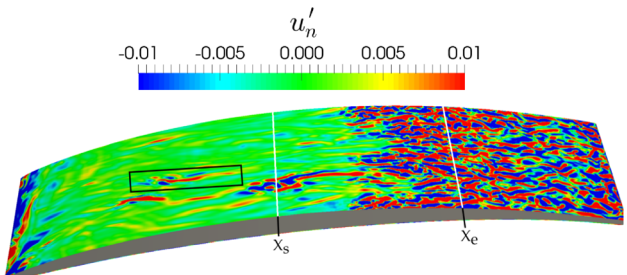


Fig. 11 Case C5. Contours of the normal velocity perturbations, u'_n , on a plane inside the suction surface boundary layer $d^+ \approx 15$.

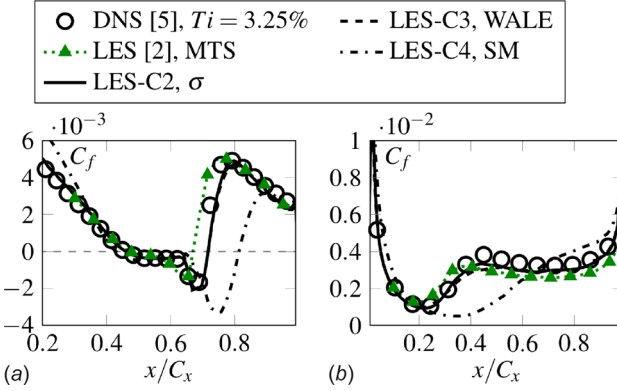


Fig. 12 Skin friction coefficient distributions for cascade 1 with inflow $Ti = 3.25\%$, with various SGS models used: (a) suction surface and (b) pressure surface

SGS viscosity. On the suction surface, the boundary layer separates earlier, leading to a significantly larger separation bubble. Figure 13(a) shows the boundary layer velocity profiles at $x = 0.4C_x$. The boundary layer is noticeably thicker in case C4, with a smaller near-wall gradient, meaning it is less able to resist the adverse pressure gradient. Figure 13(b) shows profiles of the term $u'_n \partial \bar{u}_t / \partial x_n$, which contributes to the production of turbulent shear stress $\bar{u}'_t \bar{u}'_n$. High free-stream forcing in the $Ti = 10\%$ case (C5) leads to significantly increased $u'_n \partial \bar{u}_t / \partial x_n$ in the suction surface boundary layer. The resulting shear stress leads to greater momentum transport inside the boundary layer, producing a less separation prone boundary layer. However, for cases C2 and C4, the $\bar{u}'_t \bar{u}'_n$ profiles in Fig. 13(b) are in close agreement. This suggests that the above mechanism discussed for the $Ti = 10\%$ case is not the cause of the inaccurate velocity profile for the SM model case (C4) seen in Fig. 13(a).

A more obvious difference between the two SGS models is seen when the turbulent tangential ($\bar{u}'_t \bar{u}'_t$) and shear ($\bar{u}'_t \bar{u}'_n$) stress profiles are separated into resolved and modeled/SGS (see Eq. (5)) contributions, in Fig. 14. The shear stress in the laminar boundary layer in the SM model case (Fig. 14(b)) is much larger than in the σ model case (Fig. 14(a)), and the absence of a shaded region for $\bar{u}'_t \bar{u}'_n$ indicates that this is almost entirely due to the contribution from the SM model. This additional shear stress would be expected to cause additional momentum transfer in the boundary layer, and it seems plausible that it is this term causing the large discrepancy in the suction surface predictions of cases C2 and C4.

Effect of Unsteady Turbulent Wakes

In this section, the effect of unsteady turbulent wakes on cascade 2 is examined. The free-stream turbulence is slightly lower at $Ti = 1.5\%$. Without wakes, the same transition mechanisms are

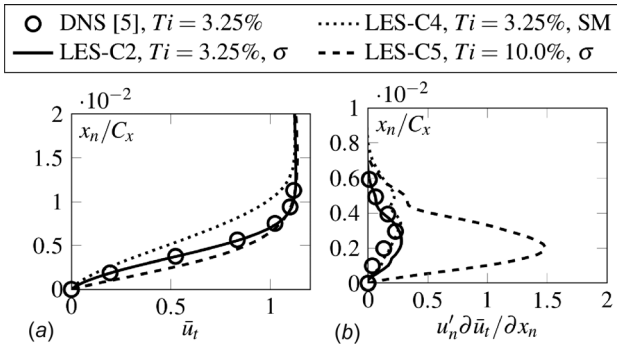


Fig. 13 Profiles of $u'_n \partial \bar{u}_t / \partial x_n$ and \bar{u}_t on the suction surface: (a) \bar{u}_t at $x/C_x = 0.4$ and (b) $u'_n \partial \bar{u}_t / \partial x_n$ at $x/C_x = 0.1$

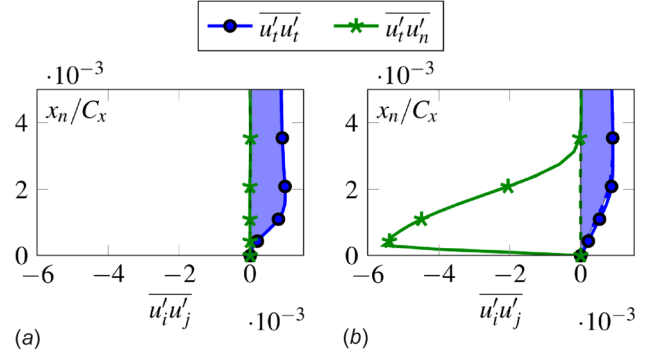


Fig. 14 Profiles of the tangential ($\bar{u}'_t \bar{u}'_t$) and shear ($\bar{u}'_t \bar{u}'_n$) components of the Reynolds stresses on the suction surface at $x/C_x = 0.025$. Solid lines show the total ($\bar{u}'_t \bar{u}'_j = \bar{u}'_t \bar{u}'_{j,SGS} + \bar{u}'_t \bar{u}'_{j,r}$) stresses, filled areas show only the resolved stresses ($\bar{u}'_t \bar{u}'_{j,r}$): (a) σ SGS model and (b) SM SGS model.

observed; the inner and overlap instabilities occur on the pressure surface, while on the suction surface, there is separation-induced transition. This “no-wake” LES case is discussed further in a previous paper [3] by the authors, where it is shown to agree well with the experimental results of Gbadebo [11].

The influence of the wakes can be elucidated by obtaining averaged quantities at a particular phase, $0 \leq \phi \leq 1$, of the wake passing period

$$\langle f \rangle(\phi) = \frac{1}{N} \sum_{n=1}^N f(t = \phi\tau + n\tau) \quad (10)$$

where $\langle \cdot \rangle$ denotes a phase-averaged quantity, τ is the wake passing period, and $N = 28$ is the total number of wake passing periods. Phase-averaged skin friction distributions are plotted in Fig. 15. On the suction surface, the skin friction distribution is seen to vary significantly as the wake passes. On the other hand, Fig. 15(b) suggests that the pressure surface transition mechanisms are not significantly influenced by the passing wakes.

The phase-dependent variation of $\langle C_f \rangle(\phi)$ on the suction surface can be seen more clearly in a phase-averaged space-time (ST) plot, presented in Fig. 16. The separation bubble region is identified by the region of negative $\langle C_f \rangle(\phi)$, and it is bounded by the separation and reattachment lines (wavy dashed lines), identified by $\langle C_f \rangle(\phi) = 0$. Throughout the wake passing period, the separation and reattachment points of the laminar separation bubble (wavy dashed lines) are seen to move away from the

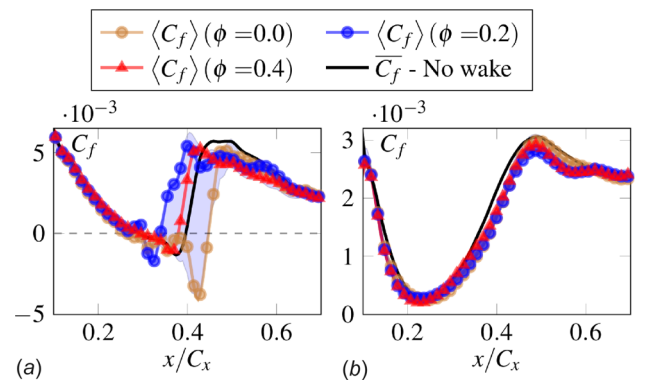


Fig. 15 Phase-averaged and time-averaged skin friction coefficient distributions for cascade 2. The filled area shows the range of $\langle C_f \rangle(\phi)$ variation throughout the wake passing period: (a) suction surface and (b) pressure surface.

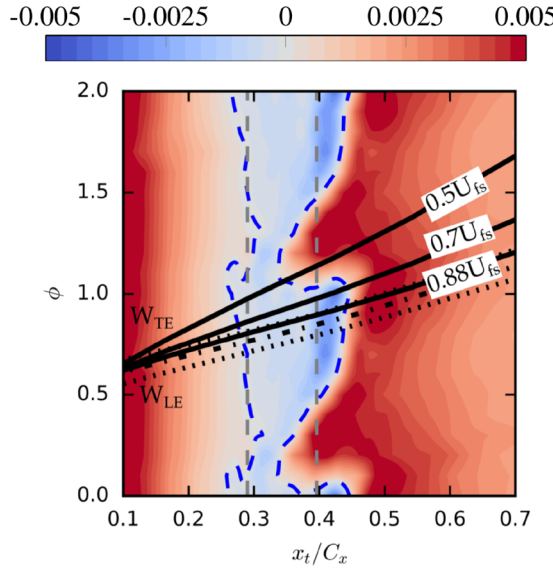


Fig. 16 Phase-averaged space-time plots of the suction surface boundary layer skin friction coefficient C_f . The dotted lines annotated with W_{LE} and W_{TE} represent the leading and trailing edges of the wake. For clarity the range $0 \leq \phi \leq 1$ is repeated to $1 \leq \phi \leq 2$.

time-averaged locations in the case without wakes (vertical dashed lines). As a result, the bubble length fluctuates from a maximum of $0.177C_x$ to a minimum of $0.043C_x$, compared to a length of $0.105C_x$ in the case without wakes. Figure 16 shows that the center of the wake passes $x = 0.44C_x$ at $\phi = 0.88$, but the reattachment point is not brought forward until $\phi = 1.01$. To explain this lag, celerity lines of $0.5U_{fs}$, $0.7U_{fs}$, and $0.88U_{fs}$ are overlaid. U_{fs} is taken as the free-stream (edge of time-averaged boundary layer) velocity magnitude, with the edge of the boundary layer detected using a vorticity magnitude threshold [2,15]. The celerity lines are positioned to originate from where the phase-averaged C_f indicates the first appearance of turbulent disturbances ($x = 0.06C_x$). The $0.88U_{fs}$ and $0.5U_{fs}$ celerity lines are important, because these are the approximate convection rates of a turbulent spot leading and trailing edge [8]. Coull and Hodson [8] showed that the strongest wake-induced disturbances on a turbine blade, which they demonstrated are amplified Klebanoff streaks, also convect at this speed.

The early reattachment induced by the wake is bounded by the $0.5U_{fs}$ and $0.7U_{fs}$ celerity lines. This suggests that wake-induced disturbances, originating from near the leading edge, convect at approximately $0.7U_{fs}$. Once they reach the separation region, they initiate earlier transition in the K-H rolls, leading to earlier reattachment. This process is visualized in Fig. 17. At $\phi = 0.6$ in Fig. 17(a), amplified Klebanoff streaks have been induced by the passing wake, but they are lagging some distance behind due to their slower convection speed. In Fig. 17(b), these amplified Klebanoff streaks are seen to initiate a turbulent spot, via the negative velocity streak lift-off mechanism discussed previously. This spot continues to grow as it convects downstream, and eventually causes the K-H rolls to transition earlier, leading to the reattachment point moving upstream.

Figure 16 shows that, after the trailing edge of the wake-amplified Klebanoff streaks (traveling at $0.5U_{fs}$) have convected past, a relatively slow drop in shear stress occurs. Eventually, the reattachment line moves downstream of its wake-free location. This is characteristic of the calmed region that has been found to follow turbulent spots [30].

The cascade 1 time-averaged C_p and C_f distributions were shown to be close to grid independent on the baseline mesh, and the cascade 2 mesh was designed to the same nondimensional

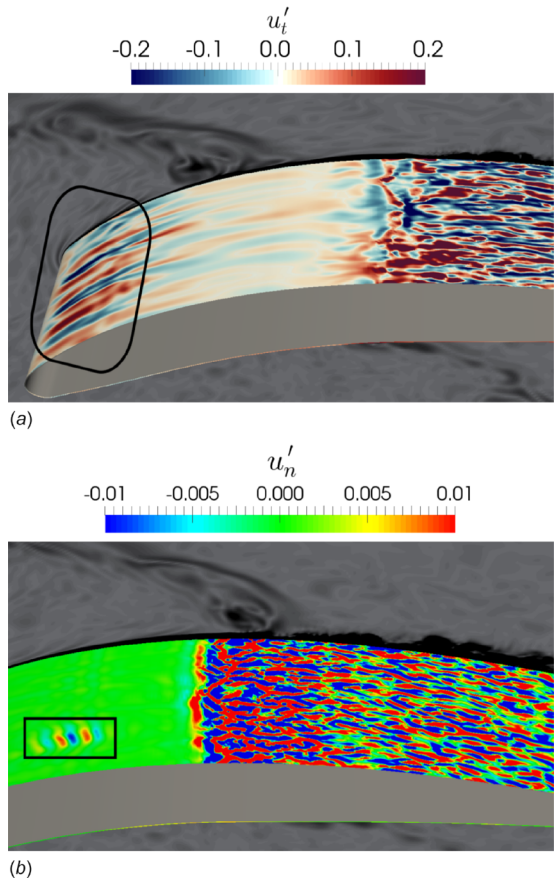


Fig. 17 Contours of the tangential and normal velocity perturbations ($f'(\phi) = f - \langle f \rangle(\phi)$) on the suction surface $d^+ \approx 15$ plane. To show the passing wake, contours of instantaneous vorticity magnitude are shown at $z = 0$ (in the background): (a) tangential velocity perturbations, $\phi = 0.6$ and (b) normal velocity perturbations $\phi = 0.8$.

wall spacing limits.² Furthermore, the suction and pressure surface transition mechanisms in cascade 1 have been shown to be closely related to Klebanoff streaks. Since the wake-induced transition in cascade 2 has also been demonstrated to be caused by wake-amplified Klebanoff streaks, this adds confidence to the results presented here.

Conclusions

The following conclusions are drawn from this study:

- (1) With the proposed LASW scheme, and a suitable SGS model, LES is able to give predictions that are in good agreement with DNS. The LASW scheme minimized the numerical dissipation while preventing dispersive errors, avoiding the need for manual tuning with reference to a priori data.
- (2) In addition to giving good mean flow predictions, the LES has been found to accurately capture the complex transition mechanisms. The inner and overlap modes, observed by Zaki et al. [5], were well replicated by the LES. Although still influenced by the Klebanoff streaks, these modes do not resemble the traditional mechanism observed in DNS of bypass transition [28]. The sensitivity to free-stream turbulence intensity is also well captured.
- (3) Despite studies reporting the poor performance of the Smagorinsky–Lilly SGS model in transitional flows [31], it

² $\Delta^+ < 50/1/15$ in the streamwise, wall-normal, and spanwise directions.

- is still commonly used. This study confirmed that the model is unsuitable for these flows. The excessive SGS viscosity in the laminar boundary layers leads to premature separation on the suction surface, and it damps the inner and overlap instabilities on the pressure surface. Encouragingly, the WALE and Sigma models perform much better here, and offer a promising alternative to more involved models such as the dynamic Smagorinsky approach.
- (4) Incoming turbulent wakes amplified Klebanoff streaks in the laminar boundary layers. The streaks were found to instigate turbulent spots, which periodically shorten the suction surface separation bubble. The 70% of free-stream celerity line, associated with the convection speed of the amplified Klebanoff streaks, was found to be important here. This has similarities with the wake-induced transition mechanism in turbine flows, reported by Coull and Hodson [8].
- ### Acknowledgment
- This work was supported by the EPSRC through an iCASE award sponsored by Rolls-Royce plc. Rolls-Royce plc are gratefully acknowledged for allowing the use and modification of their CFD solver *Hydra*.³ Finally, the authors would like to thank Dr. Naqavi, Dr. Watson, and Mr. Cui for their invaluable inputs, Dr. Zaki for providing the geometry for cascade 1, and Dr. Lardeau for providing the inflow turbulence code.
- ### Funding Data
- ARCHER UK National Supercomputing Service under Engineering and Physical Sciences Research EPSRC grant (EP/L000261/1, Funder ID. 10.13039/501100000266).
- ### Nomenclature
- C = blade chord
 C_f = skin friction coefficient, $\mu_l(\tau_w)/((1/2)\rho U_1^2)$
 C_p = static pressure coefficient,
 $(p - p_1)/((1/2)\rho U_1^2)$
 C_x = blade axial chord
 d = wall distance
 h = blade height/span
 H = boundary layer shape factor, δ^*/θ
 i = incidence angle
 k = turbulent kinetic energy
 L = integral length scale of turbulence
 L_e = dissipation length scale of turbulence
 $\Delta\sqrt{\tau_w/\rho}/\nu$
 Q = Q-criterion $(1/2)(|\Omega|^2 - |\mathbf{S}|^2)$
 Re = Reynolds number
 S = blade pitch
 \mathbf{S} = magnitude of strain rate tensor, $\sqrt{2S_{ij}S_{ij}}$
 Ω = magnitude of vorticity tensor, $\sqrt{2\Omega_{ij}\Omega_{ij}}$
 S_{ij}/Ω_{ij} = strain rate/vorticity tensors
 t = blade thickness
 T_i = free-stream turbulence intensity
 T^* = flow through time
 $u_{rms}, v_{rms}, w_{rms}$ = streamwise, wall-normal and spanwise rms velocities
 u_τ = friction velocity, $\sqrt{\tau_w/\rho}$
 U_1 = inflow bulk velocity
 U'_{RMS} = rms mean velocity, $\sqrt{1/2(u_{rms}^2 + v_{rms}^2 + w_{rms}^2)}$
 x, y, z = axial, pitchwise, spanwise co-ordinates
- Y_p = total pressure loss coefficient
 $(p_0 - p_1)/((1/2)\rho U_1^2)$
 α_2 = exit flow angle
 δ_0 = boundary layer thickness based on $0.99U_1$
 Δ_{SGS} = subgrid scale model filter
 Δ_{vol} = cell volume filter, $\sqrt[3]{\Delta x \Delta y \Delta z}$
 δ^* = boundary layer displacement thickness
 Δ^+ = nondimensional grid spacing at wall,
 $\Delta\sqrt{\tau_w/\rho}/\nu$
 ε = turbulent dissipation
 θ = boundary layer momentum thickness
 μ_{sgs} = subgrid scale viscosity
 μ_l/μ_t = laminar/turbulent viscosity
 $\sigma_{1/2/3}$ = singular values of the resolved velocity gradient tensor
- ### Subscripts
- FS = free-stream quantity
 1 = inflow quantity
 2 = exit quantity
- ### Superscripts
- FST = free-stream turbulence
KH = Kelvin–Helmholtz
LBL = laminar boundary layer
MTS = mixed time-scale
rms = root-mean-square
SGS = subgrid scale
TBL = turbulent boundary layer
TD = turbulent dissipation
TS = Tollmien–Schlichting
VD = viscous dissipation
- ### References
- [1] Steinert, W., and Starken, H., 1996, "Off-Design Transition and Separation Behavior of a CDA Cascade," *ASME J. Turbomach.*, **118**(2), pp. 204–210.
 - [2] Lardeau, S., Leschziner, M., and Zaki, T., 2011, "Large Eddy Simulation of Transitional Separated Flow Over a Flat Plate and a Compressor Blade," *Flow Turbul. Combust.*, **88**(1–2), pp. 19–44.
 - [3] Scillitoe, A. D., Tucker, P. G., and Adami, P., 2016, "Numerical Investigation of Three-Dimensional Separation in An Axial Flow Compressor: The Influence of Freestream Turbulence Intensity and Endwall Boundary Layer State," *ASME J. Turbomach.*, **139**(2), p. 021011.
 - [4] Adamczyk, J. J., Hansen, J. L., and Prahst, P. S., 2007, "A Post Test Analysis of a High-Speed Two-Stage Axial Flow Compressor," *ASME Paper No. GT2007-28057*.
 - [5] Zaki, T. A., Wissink, J. G., Rodi, W., and Durbin, P. A., 2010, "Direct Numerical Simulations of Transition in a Compressor Cascade: The Influence of Free-Stream Turbulence," *J. Fluid Mech.*, **665**, pp. 57–98.
 - [6] Menter, F. R., Langtry, R., and Völker, S., 2006, "Transition Modelling for General Purpose CFD Codes," *Flow Turbul. Combust.*, **77**(1–4), pp. 277–303.
 - [7] Leggett, J., Priebe, S., Shabbir, A., Sandberg, R., Richardson, E., and Michelassi, V., 2017, "Loss Prediction in An Axial Compressor Cascade at Off-Design Incidences With Free Stream Disturbances," *ASME Paper No. GT2017-64292*.
 - [8] Coull, J. D., and Hodson, H. P., 2011, "Unsteady Boundary-Layer Transition in Low-pressure Turbines," *J. Fluid Mech.*, **681**, pp. 370–410.
 - [9] Medic, G., Zhang, V., Wang, G., Joo, J., and Sharma, O. P., 2016, "Prediction of Transition and Losses in Compressor Cascades Using Large-Eddy Simulation," *ASME J. Turbomach.*, **138**(12), p. 121001.
 - [10] Gao, F., Zambonini, G., Boudet, J., Ottavy, X., Lu, L., and Shao, L., 2015, "Unsteady Behavior of Corner Separation in a Compressor Cascade: Large Eddy Simulation and Experimental Study," *Proc. Inst. Mech. Eng. Part A: J. Power Energy*, **229**(5), pp. 508–519.
 - [11] Gbadabo, S. A., 2003, "Three-Dimensional Separations in Compressors," Ph.D. thesis, University of Cambridge, Cambridge, UK.
 - [12] Hilgenfeld, L., and Pfitzner, M., 2004, "Unsteady Boundary Layer Development Due to Wake Passing Effects on a Highly Loaded Linear Compressor Cascade," *ASME J. Turbomach.*, **126**(4), pp. 493–500.
 - [13] Piomelli, U., and Chasnov, R., 1996, "Large-Eddy Simulations: Theory and Applications," *Turbul. Transition Model.*, **2**, pp. 2269–336.
 - [14] Crumpton, P., Moinier, P., and Giles, M., 1997, "An Unstructured Algorithm for High Reynolds Number Flows on Highly Stretched Grids," *Numerical Methods Laminar Turbulent Flow*, Swansea, Wales, pp. 1–13.
 - [15] Cui, J., Nagabushana Rao, V., and Tucker, P., 2015, "Numerical Investigation of Contrasting Flow Physics in Different Zones of a High-Lift Low-Pressure Turbine Blade," *ASME J. Turbomach.*, **138**(1), p. 011003.

³<http://www.archer.ac.uk>

- [16] Rogers, S. E., Kwak, D., and Kiris, C., 1991, "Steady and Unsteady Solutions of the Incompressible Navier-Stokes Equations," *AIAA J.*, **29**(4), pp. 603–610.
- [17] Roe, P., 1986, "Characteristic-Based Schemes for the Euler Equations," *Annu. Rev. Fluid Mech.*, **18**(1), pp. 337–365.
- [18] Tajallipour, N., Babaee Owlam, B., and Paraschivoiu, M., 2009, "Self-Adaptive Upwinding for Large Eddy Simulation of Turbulent Flows on Unstructured Elements," *J. Aircr.*, **46**(3), pp. 915–926.
- [19] Bassenne, M., Urzay, J., Park, G. I., and Moin, P., 2016, "Constant-Energetics Physical-Space Forcing Methods for Improved Convergence to Homogeneous-Isotropic Turbulence With Application to Particle-Laden Flows," *Phys. Fluids*, **28**(3), p. 035114.
- [20] Smagorinsky, J., 1963, "General Circulation Experiments With the Primitive Equations," *Mon. Weather Rev.*, **91**(3), pp. 99–164.
- [21] Schumann, U., 1975, "Subgrid Scale Model for Finite Difference Simulations of Turbulent Flows in Plane Channels and Annuli," *J. Comput. Phys.*, **18**(4), pp. 376–404.
- [22] Nicoud, F., and Ducros, F., 1999, "Subgrid-Scale Stress Modelling Based on the Square of the Velocity Gradient Tensor," *Flow Turbul. Combust.*, **62**(3), pp. 183–200.
- [23] Nicoud, F., Toda, H. B., Cabrit, O., Bose, S., and Lee, J., 2011, "Using Singular Values to Build a Subgrid-Scale Model for Large Eddy Simulations," *Phys. Fluids*, **23**(8), p. 085106.
- [24] Saad, T., Cline, D., Stoll, R., and Sutherland, J. C., 2016, "Scalable Tools for Generating Synthetic Isotropic Turbulence With Arbitrary Spectra," *AIAA J.*, **55**(1), pp. 1–14.
- [25] Bailly, C., and Juve, D., 1999, "A Stochastic Approach to Compute Subsonic Noise Using Linearized Euler's Equations," *AIAA Paper No. 99-1872*.
- [26] Wu, X., Jacobs, R. G., Hunt, J. C. R., and Durbin, P. A., 1999, "Simulation of Boundary Layer Transition Induced by Periodically Passing Wakes," *J. Fluid Mech.*, **398**, pp. 109–153.
- [27] Saric, W. S., 1994, "Gortler Vortices," *Annu. Rev. Fluid Mech.*, **26**(1), pp. 379–409.
- [28] Jacobs, R. G., and Durbin, P. A., 2001, "Simulations of Bypass Transition," *J. Fluid Mech.*, **428**, pp. 185–212.
- [29] Zaki, T. A., and Durbin, P. A., 2006, "Continuous Mode Transition and the Effects of Pressure Gradient," *J. Fluid Mech.*, **563**, pp. 357–388.
- [30] Cumpsty, N. A., Dong, Y., and Li, Y. S., 1995, "Compressor Blade Boundary Layers in the Presence of Wakes," *ASME Paper No. 95-GT-443*.
- [31] Sayadi, T., and Moin, P., 2012, "Large Eddy Simulation of Controlled Transition to Turbulence," *Phys. Fluids*, **24**(11), p. 114103.